J Mater Sci (2007) 42:4763–4771
DOI 10.1007/s10853-006-0618-2

Microstructure evolution of laser surface remelted Zn-2.7 wt.%Cu hyperperitectic alloy

Yunpeng Su · Xin Lin · Sen Yang · Meng Wang · Weidong Huang

Received: 9 September 2005 / Accepted: 26 June 2006 / Published online: 19 March 2007

Abstract Laser surface remelting experiments on Zn-2.7 wt.%Cu hyperperitectic alloy were performed by using a 5kW CW CO_2 laser at beam scanning velocities ranging between 6 and 1,207 mm/s. With the increase of the growth rate, the microstructures of Zn-2.7 wt.% Cu alloy changed from planar interface to lamellar structures, cellular structures, and finally to high velocity absolute stability (HVAS) planar interface at a growth rate of 349 mm/s. The critical growth rate for the transformation from lamellar structure to cells was about 96 mm/s. Quantitative measurement was preformed to reveal the relationship between the average lamellar spacing and the corresponding growth rate, and the results are in excellent agreement with the prediction of the TMK eutectic model.

Y. Su · X. Lin · M. Wang · W. Huang
State Key Laboratory of Solidification Processing, Northwestern Polytechnical University, Xi'an 710072, P.R. China

S. Yang
Department of Materials Science and Engineering, Inner Mongolia University of Technology, Hohhot 010051, P.R. China

Y. Su (✉)
Department of Industrial and Systems Engineering, The Hong Kong Polytechnic University, Hung Hom, Kowloon, Hong Kong
e-mail: zhangyangqiansyp@yahoo.com.cn

Introduction

Solidification is one of the most important processing routes for many materials, especially metals and alloys. Solidification microstructures depend on many parameters, especially on growth rate, local temperature gradient and material composition. As the peritectic reaction is present in many technologically important material systems, microstructure evolution of peritectic alloys has attracted a lot of attentions over the past three decades. Experimental and theoretical studies on peritectic alloys at low or medium growth rate have been performed [1–6] and several new morphologies, such as lamellar structures, low speed banded structures etc., have been observed. However, until now, there have been few experiments on the microstructure selection of peritectic alloy under rapid unidirectional solidification and ultra-high temperature gradient conditions, especially near the absolutely stability. The understanding on the microstructure evolution under such conditions is still very poor.

During laser surface remelting, temperature gradient in the molten pool can be extremely high, and unidirectional solidification can be achieved at very high growth rate if processing parameters are properly controlled [7]. The growth rate can be simply determined [8] and the local temperature gradient can also be calculated numerically [9].

In the present paper, systematic experimental research on laser rapid unidirectional solidification of Zn-2.7 wt.%Cu hyperperitectic alloy has been carried out by using laser surface remelting technique. The main purpose of the present study is to investigate the microstructure evolution of 2.7 wt.%Cu hyperperitectic

alloy under the condition of rapid solidification and ultra-high temperature gradient conditions.

Experimental

Zn-2.7 wt.% Cu alloy specimens with the square of 14 mm and the length of 92 mm were prepared by melting pure 99.995% Zn and pure 99.9999% Cu under Ar atmosphere in an induction furnace and then cut into samples of 6 mm × 12 mm × 30 mm used for laser remelting experiments. All the samples were ground on 500 grit SiC paper and thoroughly cleaned in acetone in order to reduce the reflectivity for the laser beam and obtain a similar surface quality for each one. In addition, the alloy composition of the samples measured by Electron Probe Microanalysis (EPMA) was between 2.63 and 2.75 wt.%Cu. The binary phase diagram of Zn-rich Zn–Cu alloys is shown in Fig. 1.

All laser surface remelting experiments were carried out by using on a Rofin-Sinar 850 5 kW CW CO_2 laser at various scanning velocities between 6 mm/s and 1,207 mm/s by employing a uniform straight-line motion mechanism with a hover guide track. The hover guide track is a kind of track which provides a resistance-free condition for samples moving on it by using air suspension technique. The laser beam was focused on a spot of 0.5 mm in the diameter and had a power density of 1.0×10^6 W/cm^2. A continuous flow of He (10 L/min) was blown onto the melting zone to prevent heavy oxidation during the laser treatment. In order to protect the operators from Zinc poisoning, a gas extractor with a filter was placed near the samples. Longitudinal and transverse cross sections of the samples were cut and microstructures were analyzed by optical microscope and SEM technique. In addition, the average composition in the molten pool was measured by EPMA. The results of EPMA showed that the average concentration of Cu in the molten pool slightly decreased from 3.05 wt.% to 2.80 wt.% with the increase of scanning velocities from 6 mm/s to 1,204 mm/s. Local growth velocity V_s could be simply related to the scanning velocity V_b via the relationship $V_s = V_b\cos\theta$ [8], where θ is the acute angle between the direction of V_b and V_s. In this paper, the angle θ was measured by a sampling method similar to the one adopted by Pan [11] and us [12], as illustrated in Fig. 2.

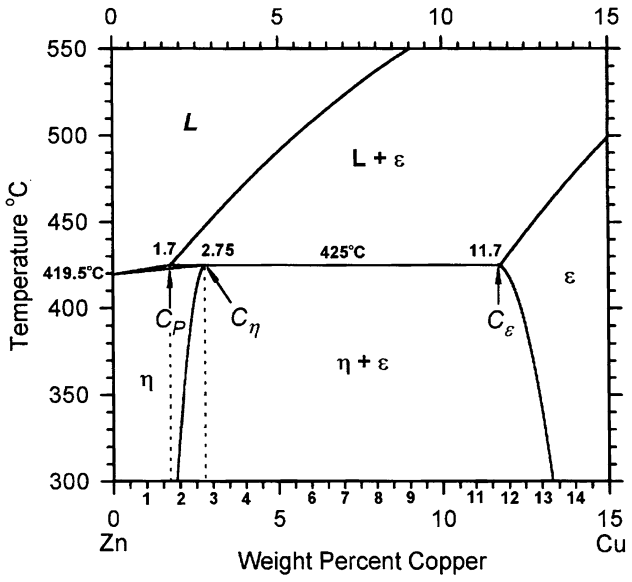

Fig. 1 Binary phase diagram of Zn-rich Zn–Cu alloys [10]

Results

Typical microstructures

Optical micrograph of the laser molten pool at a scanning velocity of 10 mm/s was shown in Fig. 3. It can be seen that the typical microstructure of the substrate is the dendrite and the average grain size is larger than 100 μm. Four typical microstructures were identified in the laser molten pools of the Zn-2.7 wt.%Cu alloy at scanning velocities ranging from 6 mm/s to 1,207 mm/s. With the increase of growth rate, the microstructures of Zn-2.7 wt.%Cu alloy changed from featureless structures to lamellar structures, cellular structures, and finally to absolute stability planar interface structures. The SEM micrographs (secondary electron mode) of the aforementioned typical microstructures were shown in Fig. 4. The black arrows in the top of the figures indicate the direction of scanning velocity, V_b. A narrow band consists of featureless structures can be seen at the bottom of the molten pool (The narrow band "A" in

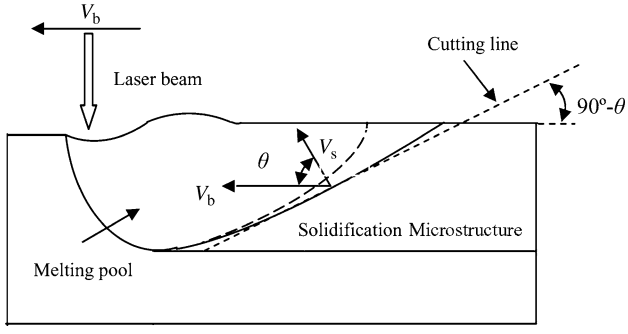

Fig. 2 Schematic diagram of cutting specimens

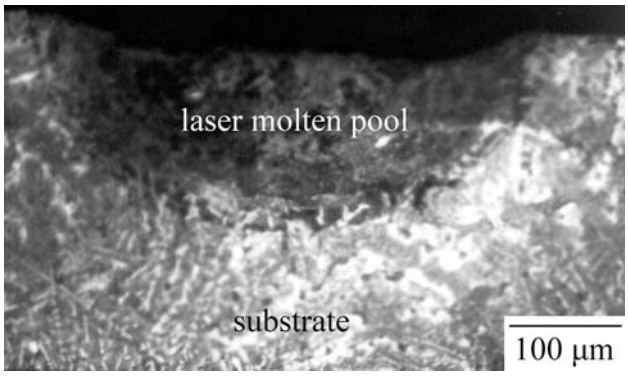

Fig. 3 Optical micrograph of the laser molten pool at a scanning velocity of 10 mm/s

Fig. 4a), which resulted from the planar interface growth of η phase at low growth rate and extremely high temperature gradient. As the remelting time in the bottom of laser molten pool is transitory, partially remelted as-cast ε dendrites can be observed on the edge of laser molten pool. The lamellar structure, which consists of gray (η phase) and black layers (ε phase) is found to grow originally from the featureless structures and then protrude into the remelted zone, as shown in Fig. 4a. This structure is similar to the structure found in the Bridgman samples grown at velocities ranging from 2.0 mm/s to 6.4 mm/s for the same alloy [13]. It can be clearly seen that the growth direction of the lamellar structures does not gradually change with increasing distance from the bottom, but almost keeps constant within a considerably wide area. It is well known that the direction of local temperature gradient in the molten pool changes gradually with the increase of the distance from the bottom of the molten pool [14]. This result indicates that the growth direction of the growing lamellar structures is mainly determined by the preferred crystal orientation rather than the heat flow direction. With the increase of growth rate, the lamellar structure became more regular (Fig. 4b). When the scanning velocity reached about 96.0 mm/s, the lamellar structure transformed into an irregular structure with larger width and shallower grooves, as shown in Fig. 4c. In our previous paper [12], this structure was identified as thin cellular structure of η phase. That is to say, lamellar-cellular transition was observed and the experimentally determined critical velocity was about 96.0 mm/s. As the growth rate is increased further to a certain value, cells in the molten pool disappeared (as shown in Fig. 4d). Comparing them with the cells in the same section (longitudinal) at relatively low growth rate (see Fig. 4c), one can clearly find that the cell boundaries completely disappeared and a fully cell-free microstructure was obtained.

Lamellar spacing

Lamellar spacing was measured on polished and etched sections perpendicular to the growth direction. Figure 5 gives the average lamellar spacing, $\bar{\lambda}$, maximum spacing, λ_{max}, and minimum spacing, λ_{min}. Some experimental laws can be obtained as follows:

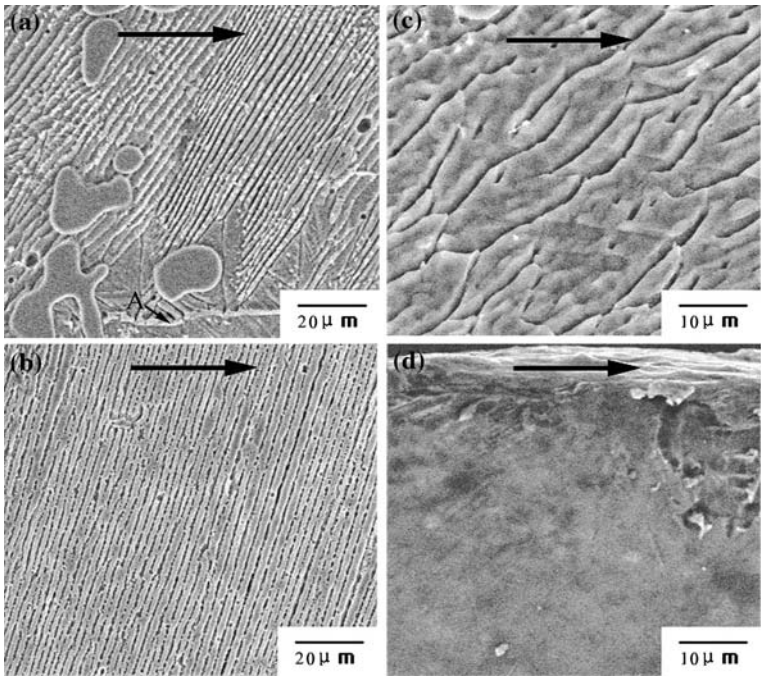

Fig. 4 Typical microstructures from longitudinal cross section of Zn-2.7%Cu alloy under different solidified velocities of (**a**) V_s = 4.4 mm/s, (**b**) V_s = 24.0 mm/s, (**c**) $V_s \approx$ 96.5 mm/s, (**d**) $V_s \approx$ 349.0 mm/s, respectively

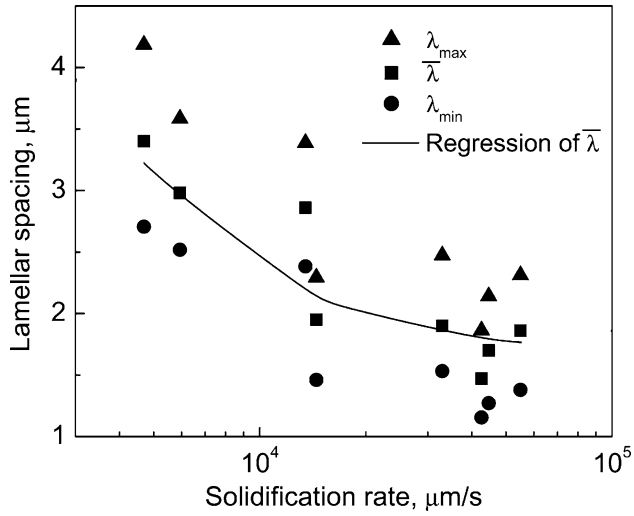

Fig. 5 Relationship of lamellar spacing to solidification rate V_s given by experimental method

(1) There existed a distribution range in primary spacing under rapid solidification conditions. The effect of the growth rate on the ratio of the maximum spacing to the minimum spacing was unremarkable.
(2) The average lamellar spacing ($\bar{\lambda}$) of lamellar structures decreased from 3.4 μm to 1.5 μm with increasing growth rate from 3.6 mm/s to 65.2 mm/s, and then increased to 1.9 μm with growth rate increasing to 91.1 mm/s.
(3) Nonlinear regression analysis of the experimental results gave the relationship between $\bar{\lambda}$ and V_s as

$$\bar{\lambda}V_s^{1/2} = 0.00384V_s + 200.14 \quad (1)$$

where the R^2 was 0.80197.

Discussion

Calculation of IRF

The phase and pattern selection during solidification depends on alloy composition and solidification conditions. There are a lot of nonlinear coupling factors which should be treated, if one tries to give a completely quantitative description of pattern and phase selection of peritectic alloy during solidification. It should be a difficult task for a technical reason. However, in many cases, the application of the maximum interface temperature criterion to the constrained growth leads to quite satisfactory results. Generally, during directional solidification, because of the similarity of crystal lattice and lattice constant, the nucleation undercooling for one phase nucleated in the other phase is quite small. It is believed that the phase or the pattern with a higher interface temperature is more stable in kinetics and will be dominant in the final microstructure [15]. In our experiments, unidirectional solidification was achieved by using laser surface remelting technique and the nucleation process generally can be ignored during solidification (epitaxial growth). So the maximum interface temperature criterion was employed to predict the microstructure evolution of the Zn-2.7 wt.%Cu alloy during laser surface remelting. In order to determine the dominant growing interface, the growth temperatures of all possible phases and growth patterns have been calculated. These interface temperatures, which are functions of growth rate and temperature gradient for a given alloy, are called interface response functions (IRF). The relevant growth patterns in this paper are plane front structures, cells/dendrites and lamellar structures.

Single phase plane front growth

With assuming linear attachment kinetics and dilute solutions, the growth temperature of a single phase planar front was given by ref. [16–18]

$$T_P(V_s) = T_f + C_1^* m_v - (R_g T_f/\Delta S_f)V_s/V_C \quad (2)$$

$$k_V = \frac{k_e + \alpha_0 V_s/D_i}{1 + \alpha_0 V_s/D_i} \quad (3)$$

$$m_v = \frac{1 - k_v[1 - \ln(k_e/k_v)]}{1 - k_e} m \quad (4)$$

where T_f is the melting temperature of the pure component, $C_1^* = C_0/k_V$ is the concentration of the liquid at the interface, R_g is the gas constant, ΔS_f is the molar entropy of fusion, and V_C is the limit of crystallization, which has an upper bound equal to the velocity of sound. In an equilibrium state, T_p corresponds to the solidus temperature for the initial composition, C_0.

Cellular/dendritic growth

The IRF of both η and ε cellular structures have been calculated by using Lin Xin's self-consistent numerical model for single-phase solidification represented in our previous papers [19, 20]. This numerical model extended the Hunt-Lu cellular/dendritic growth numerical model [21] and was further developed to describe the complete morphology evolution from the

constitutional under cooling limit (CUL) to the absolute stability limit (ASL) during unidirectional solidification. This numerical model can be described as follows.

With considering an axisymmetric interface shape and neglecting the effect of convection, we set a moving coordinate system fixed to the experimental sample in a directional solidification system. The temperature field is assumed to be linear for the reason that usually the solidification latent heat is small and the heat conductivity is large. Then the temperature field is defined as

$$T_i = T_0 + G_T z \tag{5}$$

where T_0 is the liquidus temperature for the mean composition of the bulk alloy composition C_0, G_T is the imposed temperature gradient at the interface, z is the axial position in a coordinate system moving at the pulling velocity V_0 and this coordinate system is referred to as the gradient coordinate system. The solute distribution in the liquid and solid is determined by the following diffusion equations corresponding to the above moving coordinates, respectively:

$$D_L \nabla^2 C_L + V_0 \frac{\partial C_L}{\partial z} = \frac{\partial C_L}{\partial t} \tag{6}$$

$$D_S \nabla^2 C_S + V_0 \frac{\partial C_S}{\partial z} = \frac{\partial C_S}{\partial t} \tag{7}$$

where C_L, C_S are the solute concentration for liquid and solid, respectively, and D_L, D_S are the solute diffusivity for liquid and solid, respectively. The solute concentrations for the liquid and the solid should also satisfy the following far field conditions:

$$C_L = C_0, \text{ at } z \to +\infty \tag{8}$$

$$\frac{\partial C_S}{\partial z} = 0, \text{ at } z \to -\infty \tag{9}$$

At the interface:

$$C_{Si} = k_V C_{Li} \tag{10}$$

$$V_n(k_V - 1)C_{Li} = D_L \frac{\partial C_L}{\partial n} - D_S \frac{\partial C_S}{\partial n} \tag{11}$$

where V_n is the growth velocity in the normal direction.

The temperature field and the concentration field at the interface must satisfy the Gibbs-Thomson equation

$$T_i = T_0 + m(C_{Li} - C_0) - \Gamma\left(\zeta\frac{1}{R_1} + \frac{1}{R_2}\right) - \frac{V_n}{\mu} \tag{12}$$

where $\xi = 1–\alpha_n\cos(n\theta)$, θ is the angle between the interfacial normal and the dendrite growth direction, n is the rotational symmetry degree of the alloy crystal lattice, α_n is the anisotropic coefficient, Γ is the Gibbs-Thomson coefficient, R_1 and R_2 are the main curvature radii at the interface, $\mu = V_C\Delta S_f/(R_g T_i)$ is the kinetic coefficient.

By employing the cell/dendrite shape calculated by the Hunt-Lu model as a initial interface shape, the diffusion Eqs. (5) ~ (12) are solved by the finite-difference method through control volume integration discretization. A self-consistent interface shape can be obtained by coupling the temperature field with the solute field along the solid/liquid interface through Eq. (12). Based on the fact that the dendritic arrays in directional solidification usually have a hexagonal structure of axial symmetry, only a symmetry unit of a dendrite has been taken into consideration in the numerical calculation, which is half of the dendrite unit. The model has included composition distribution information in both liquid and solid phases and some major morphological factors, such as tip undercooling, tip radius, primary spacing, stable shape of the dendrite etc.

Lamellar structures

Perepezko [22] suggested that a metastable eutectic reaction might be exposed if undercooling was sufficient in some alloys. The subsequent experiments performed by Liu [23] and us [12, 13] have identified the transformation from a peritectic to metastable eutectic reaction as the inherent reason for the formation of lamellar structures in peritectic alloy. That is to say, the lamellar structure in peritectic alloy is a kind of metastable eutectic structure. So the TMK eutectic model for high growth rate [24] has been employed to calculate IRF of the lamellar structure. The parameters used for the calculation are listed in Table 1.

IRF

Figure 6a shows the IRF of both cell/dendrite of the ε and η phases and lamellar structures in Zn-2.7Cu

Table 1 Parameters for Zn-Cu diagram and thermophysical data of the phases involved solidification procedure

Parameters	Symbol	Value	Reference
Melting point of Zn	T_{Zn}	692.73 K	[25]
Melting point of Cu	T_{Cu}	1358.02 K	[25]
Difference in composition between the end of the eutectic tie-line①	C'	2.47 wt.%	
Gibbs-Thompson coefficient of ε phase	Γ_ε	1.1×10^{-7} K m	[26]
Gibbs-Thompson coefficient of η phase	Γ_η	1.1×10^{-7} K m	[26]
Volume fraction of ε phase②	F	0.18	
Nonequilibrium liquidus slope of ε phase①	m_ε	18 K/wt.%Zn	
Nonequilibrium liquidus slope of η phase①	m_η	–0.5 K/wt.%Zn	
Equilibrium distribution coefficient of ε phase	k_ε	0.65	[25]
Equilibrium distribution coefficient of η phase (corrected)	k_η	0.62	[26]
Diffusion coefficient in liquid	D_L	2.04×10^{-9} m^2/s	[25]
Diffusion coefficient in solid	D_S	1.59×10^{-12} m^2/s	[27]
Peritectic temperature	T_p	698.14 K	[26]
Liquid composition at peritectic reaction	C_l	1.7 wt.%Cu	[26]
Composition in primary ε at peretectic reaction	C_ε	11.7 wt.%Cu	[25]
Composition in peritectic η at peretectic reaction	C_η	2.75 wt.%Cu	[25]
Equilibrium liquidus slope of ε phase	m_ε	–17.1 K/wt.%Zn	[25]
Equilibrium liquidus slope of η phase	m_η	–3.19 K/wt.%Zn	[25]
Limit of crystallization of ε phase	$V_{C\varepsilon}$	4304 m/s	[28]
Limit of crystallization of η phase	$V_{C\eta}$	4243 m/s	[28]

①Acquired from metastable phase diagram [12]

②Measured by Quantimet 500 Image Analysis System

hyperperitectic alloy when they solidify independently. A magnified view of the intersectant section in the dashed rectangle in Fig. 6a is also shown in Fig. 6b. In addition, the temperature gradient G_T is a typical value calculated with a semi-analytic model established by Liu et al. [9], and it has no significant effect on the IRF within the velocity range discussed in this paper. At low growth rate, the interface temperature of planar interface of the η phase is the highest one. With the increase of the solidification rate, the planar interface of the η phase is unstable and the interface temperature of lamellar structures becomes higher than that of the η phase. With the further increase of the solidification rate, the interface temperature of lamellar structures decreases gradually and becomes lower than that of cellular/dendritic structures of the η phase at a solidification rate of about 40 mm/s. It means that cellular/dendritic structures of the η phase will replace lamellar structures in the final microstructure at this solidification rate.

Transition from lamellar structure to thin cells

Several literatures have reported the microstructures transition from cells to lamellar structures, i.e., metastable eutectic structures, in Bridgman samples of the present alloys at solidification velocity in the order of 1 mm/s [29, 30]. With considering the symmetry of the microstructure evolution, there may exist a transition opposite to the aforementioned one, i.e., a transition from lamellar structures to cells, at a comparatively higher solidification rate. But this microstructure transition has never been observed before. However, in the present experiment, the lamellar structure changes to the thin cellular structure of η phase at a solidification rate of about 96.0 mm/s. It indicates that the microstructure transition from lamellar structure to cells has occurred. As shown in Fig. 6b, the interface temperature of lamellar structures becomes lower than that of cellular/dendritic structures of η phase at a solidification rate of about 40.0 mm/s. According to the maximum interface temperature criterion, the system selects high-speed cellular/dendritic growth of η phase above this solidification rate. One should note that the experimentally determined value for this transition is about 2.15 times of that predicted by the maximum interface temperature criterion. We mainly attribute this difference to the following aspects: differences between the actual metastable eutectic growth and the ideal eutectic growth assumed in the TMK eutectic model, uncertainties of thermophysical parameters acquired from the metastable phase diagram, and a kinetic requirement of the microstructure transition. As a transition of microstructure, the lamellar-cell transition needs some kind of driving

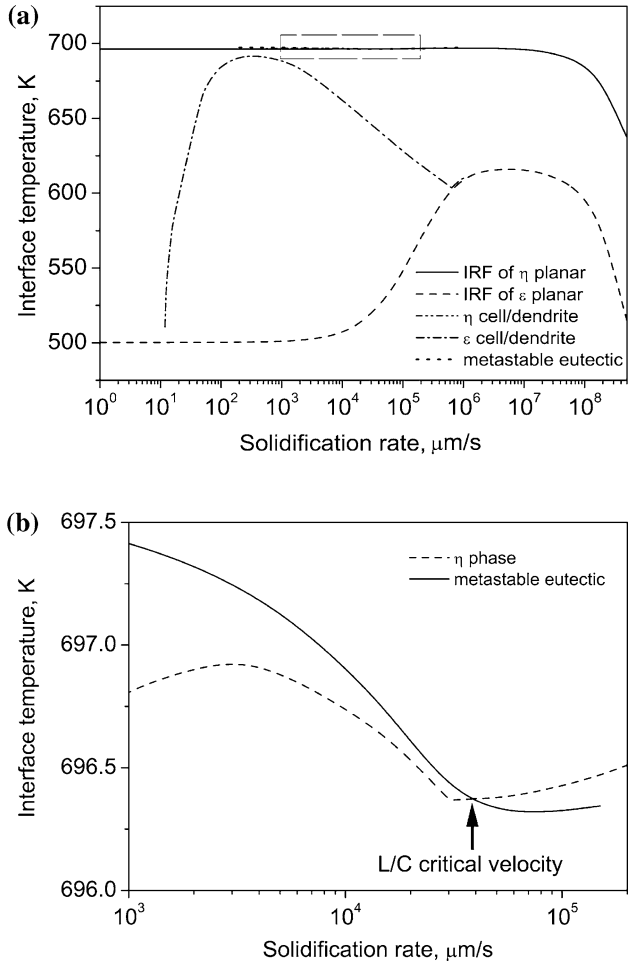

Fig. 6 IRF of the two phases in solidification of Zn-2.7 wt.%Cu alloy under temperature gradient of 5×10^5 K/m: (**a**) IRF of planar or cell/dendrite of the two phases (**b**) a magnification of the intersectant section in the dashed rectangle in (**a**)

force, i.e., the new pattern should be more kinetically preponderant than the primary one. But when the maximum interface temperature criterion is employed, we obey the implied rule that the pattern transition will occur when the two patterns are equal in the interface temperature.

Dependence of lamellar spacing on growth rate

The average lamellar spacing ($\overline{\lambda}$) of metastable eutectic structures has been calculated by using the TMK eutectic model. The regression analysis of calculated values gives the relationship between $\overline{\lambda}$ and V_s as $\overline{\lambda}V_s^{1/2} = 0.00786V_s + 217.5$, of which the R^2 is 0.99980, as illustrated in Fig. 7. The experimental results are also illustrated in Fig. 5, which are in excellent agreement with the calculated values. It indicates that the TMK eutectic model can excellently predict the lamellar spacing of metastable eutectic structures in

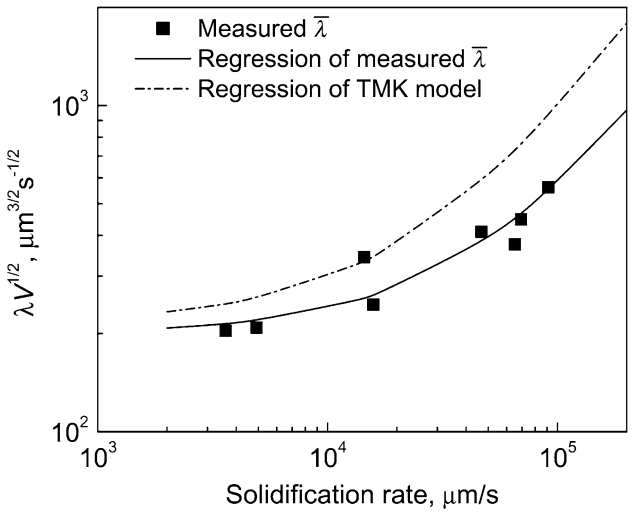

Fig. 7 Relationship of $\overline{\lambda}$ to *Vs* given by experimental measurement and calculational method with the TMK eutectic model, respectively

the peritectic alloy under ultrahigh temperature gradient and rapid solidification conditions.

The high speed absolute stability (HVAS)

Mullins and Sekerka [31, 32] first performed the rigorous linear kinetic stability analysis on the planar liquid-solid interface for a dilute binary system and low Peclet number. With their efforts, the famous M-S theory was presented in 1964, which predicted the probability of the high velocity absolute stability (HVAS). According to the M-S interface stability theory, the critical condition for HVAS is given by,

$$V_{ab} = \Delta T_0 D_L / k_e \Gamma \tag{13}$$

where k_e, Γ, D_L and ΔT_0 are the equilibrium partition coefficient, the Gibbs-Thomson coefficient, the solute diffusion coefficient and the freezing range of the alloy, respectively. For a peritectic alloy, before determining this critical velocity, we should first determine which phase is the leading phase under the local solidification condition. According to Fig. 6a, the interface temperature of the η phase is higher than that of the ε phase within the whole velocity range, so the theoretical critical velocities for the HVAS of Zn-2.7 wt.%Cu alloy can be calculated and the calculated value is 6.38×10^1 mm/s. Attention must be given to that the experimentally determined critical velocity, 3.49×10^2 mm/s (as shown in Fig. 4d), is about 5.5 times of that predicted by M-S theory. In some literatures, this kind of difference was often attributed to the effect of the possible impurity elements and the

uncertainties of the thermophysical parameters [33–37]. In fact, the nonlinear instability of the planar interface is another important reason for it.

In order to investigate the nonlinear instability of the planar interface and the dynamic bifurcation of the cellular-planar transition, an approach similar to the one adopted by Wu et al. [38] was employed. When a sinusoidal ripple perturbs the planar interface, the perturbed interface equation is

$$z = \phi(x,t) = \delta(t)\sin\omega x \tag{14}$$

where $\delta(t)$ is the amplitude of sinusoidal wave, $\omega = 2\pi/\lambda$ is the frequency, and λ is the wavelength, respectively. The equations of the changed concentration and temperature field are

$$C(x,z,t) = C_0 + \frac{G_C D}{V_s}\left[1 - \exp\left(-\frac{V_s}{D}z\right)\right] + (b - G_C)\delta\sin\omega x\exp\left(-\omega^* z\right) \tag{15}$$

$$T'(x,z,t) = T_0 + \frac{G' D'_{th}}{V_s}\left[1 - \exp\left(-\frac{V_s}{D'_{th}}z\right)\right] + (a' - G')\delta\sin\omega x\exp\left(-\omega'_{th} z\right) \tag{16}$$

$$T(x,z,t) = T_0 + \frac{G D_{th}}{V_s}\left[1 - \exp\left(-\frac{V_s}{D_{th}}z\right)\right] + (a - G)\delta\sin\omega x\exp\left(-\omega_{th} z\right) \tag{17}$$

where $C(x, z, t)$ is the instantaneous concentration of solute in the liquid phase, C_0 is the liquid phase solute concentration at the unperturbed planar interface ($\delta = 0$), $T(x, z, t)$ and T' (x, z, t) are the instantaneous temperature in the liquid phase and in the solid phase, respectively, T_0 is the temperature of the unperturbed planar interface, G_C is the concentration gradient of solute in the liquid phase at the unperturbed planar interface, D is the diffusion coefficient of solute in the liquid phase, D'_{th} and D_{th} are the thermal diffusivity of the solid and liquid phase, respectively, G' and G are the temperature gradient in the solid and liquid at the unperturbed planar interface, respectively, and

$$\omega^* = \frac{V_s}{2D} + \left[\left(\frac{V_s}{2D}\right)^2 + \omega^2\right]^{\frac{1}{2}} \tag{18}$$

$$\omega'_{th} = \frac{V_s}{2D'_{th}} - \left[\left(\frac{V_s}{2D'_{th}}\right)^2 + \omega^2\right]^{\frac{1}{2}} \tag{19}$$

$$\omega_{th} = \frac{V_s}{2D_{th}} - \left[\left(\frac{V_s}{2D_{th}}\right)^2 + \omega^2\right]^{\frac{1}{2}} \tag{20}$$

Under rapid solidification conditions, we neglect the difference between the thermal diffusivity of the solid and liquid phase and let $G_T = (k_S G' + k_L G)/(2(k_S + k_L))$, where k_S and k_L are the thermal conductivity of the solid and liquid phase, respectively. After derivation, an implicit expression of the critical solidification velocity for the cellular-planar transition has been obtained:

$$F(V_c) = m\frac{C_\infty(k_V - 1)V_c}{Dk_V} - \left(G_T + \Gamma\omega^2\right)\cdot\left(1 + \frac{V_c k_V}{D\omega^* - v_c}\right) = 0 \tag{21}$$

It means that when $V_s < V_c$ the interface is cell mode and when $V_s \geq V_c$ it is the planar interface. Since the frequency of the perturbation, ω, which can cause instability to a planar interface, covers a wide range. The so-called maximum amplification frequency, ω_{max}, which makes the increasing rate of the amplitude of perturbation a maximum, was employed. It was obtained by numerically analyzing the M-S linear equation. The results showed that ω_{max} is a function of V_s. Substituting ω_{max} into Eq. (21) and numerically solving this equation, we can get the critical velocity under a typical value of G_T in the laser molten pool [9], 5×10^5 K/m, and the value of V_c is 1.09×10^2 mm/s, which shows a much better agreement with the experimentally obtained critical velocity of 3.49×10^2 mm/s than that predicted by M-S theory.

Generally speaking, the uncertainty of the metastable phase diagram which was employed in the calculation of the IRF, the impurities in the alloys and the dissimilarities between the perfect conditions supposed the theory models and the virtual conditions should be involved in the reasons for this difference. However, as the predicted values are always smaller than the experimental ones, we held the view point that the characteristics of phase and microstructure transformation are the primary reason. Qualitatively speaking, the highest temperature criterion, M-S theory and the nonlinear analysis are all based on the assumption that the solidification process is under the steady-state condition. But in the laser surface resolidification experiments, the velocity of the interface increases from 0 to the maximum and convection also exists in the molten pool. These factors make the local solidification condition change continuously, i.e., the solidification process is under an unsteady state condition.

Consequently, all the phase and microstructure transformation occur in the unsteady state condition; the bifurcation behavior of the system must be different with that predicted by the nonlinear analysis.

Conclusions

Laser surface remelting experiments of a Zn-2.7 wt.%Cu peritectic alloy were performed on a 5 kW CW CO_2 laser with scanning velocities varying from 6 mm/s to 1,207 mm/s. It is found that the microstructures of Zn-2.7 wt.%Cu alloy change from planar interface structures to lamellar structures, cellular structures and finally to absolute stability planar interface with the increase of the growth rate. The critical velocity for lamellar-cellular transition is 96.0 mm/s, which is in a reasonable agreement with that predicted by the highest interface growth temperature criterion.

The lamellar spacing, $\overline{\lambda}$, of lamellar structures decreased from 3.4 μm to 1.5 μm with the increase of the growth rate from 3.6 mm/s to 65.2 mm/s, and then increased to 1.9 μm while the growth rate increasing to 91.1 mm/s. TMK eutectic model was employed to predict lamellar spacing and the results showed an excellent agreement with the experimentally observed lamellar spacing.

The critical velocity for high velocity absolute stability was evaluated by using a nonlinear stability criterion of the planar interface, and a much better agreement with the experimental value was achieved.

Acknowledgements This work is financially supported by the National Natural Science Foundation of China Grant No. 50201012, 50471065. The authors would like to thank Miss Qian Chen and Miss Xiaoqin Yu of Lan Zhou University of Technology for her enthusiastic help.

References

1. Chalmers B (1959) In: Physical metallurgy. Wiley, New York, p 1
2. Boettinger WJ (1974) Metall Trans A 5:2023
3. Flemings MC (1974) In: Solidification processing. McGraw-Hill, New York, p 6
4. Lee JH, Verhoeven JD (1994) J Cryst Growth 144:353
5. Busse P, Meissen F (1997) Scripta Mater 36:653
6. Vandyoussefi M, Kerr HW, Kurz W (2000) Acta Mater 48:2297
7. Yang S, Huang WD, Liu WJ, Su YP, Zhou YH (2002) Chinese J Lasers 29A:475
8. Gremaud M, Carrard M, Kurz W (1991) Acta Metall Mater 39:1431
9. Liu ZX, Huang WD, Yang S (2002) Chinese J Nonferr Metal 12:458
10. Massalski TB (1986) In: Binary alloy phase diagram. American Society for Metals, Metals Park, OH, p 235
11. Pan QY, Huang WD, Lin X, Zhou YH (1997) J Crystal Growth 181:109
12. Su YP, Lin X, Wang M, Xue L, Huang WD (2004) Scripta Materialia 51:397
13. Su YP, Wang M, Lin X, Huang WD (2004) Mater Lett 58:2670
14. Hoadley AFA, Rappaz M, Zimmermann M (1991) Metall Trans B 22:101
15. Kubin LP, Estrin Y (1985) Acta Metall 33:397
16. Trivedi R, Kurz W (1986) Int Mater Rev 39:823
17. Boettinger WJ, Coriell SR (1988) In: Sahm PR, Jones H, Adams CM (eds) NATO ASI Series E-No. 114. Martinus Nijboff, Dondrecht, p 81
18. Aziz MJ, Boettinger WJ (1994) Acta Metall Mater 42:27
19. Lin X, Li YM, Liu ZX, Li T, Huang WD (2001) Sci Techn Adv Mater 2:293
20. Lin X, Huang WD, Wang M, Li YM, Li T, Su YP, Shen SJ (2002) Sci China (Series E) 45:146
21. Hunt JD, Lu SZ (1996) Metall Mater Trans A 27:611
22. Perepezko JH, Boettinger WJ (1983) In: Bennett LH, Massalski TB, Giessen BC (eds) Mat. Res. Soc. Symp. Proc. 19. Elsevier North Holland, New York, p 108
23. Liu YC, Yang GC, Zhou YH (2002) Cryst Growth 240:603
24. Trivedi R, Magnin P, Kurz W (1987) Acta Mater 35:971
25. Massalski TB (1986) In: Binary alloy phase diagram. Metals Park, OH, p 75
26. Liu HY, Jones H (1992) Acta Metall 40:229
27. Cahn RW, Haasen P (1996) In: Physical metallurgy, 4th edn. North-Holland, Amsterdam
28. Gale WF, Totemeier TC (2004) In: Smithells metals reference book, 6th edn. Elsevier Butterworth-Heinemann, Oxford, p 14.1
29. Ma D, Li Y, Ng SC, Jones H (2001) Sci Tech Adv Mater 2:127
30. Wang M, Lin X, Su YP, Shen SJ, Huang WD (2002) Acta Metallurgica Sinica 38:37
31. Mullins WW, Sekerka RF (1963) J Appl Phys 34:323
32. Mullins WW, Sekerka RF (1964) J Appl Phys 35:444
33. Boettinger WJ, Shechtman D, Schaefer RJ et al (1984) Metall Trans A 15:55
34. Gill SC, Kurz W (1993) Mater Sci Eng A 173:335
35. Jones H (1991) Mater Sci Eng A 133:33
36. Kurz W, Giovanola B, Trivedi R (1986) Acta Metall 34:823
37. Yang S, Huang WD, Liu WJ, Zhou YH (2002) Prog Nat Sci 12:684
38. Wu JP, Hou AX, Huang DH, Bao ZY, Gao ZN, Qu SS (2001) Sci China E 44:484